Soft Matter

Micromechanical Remodeling of the Extracellular Matrix by Invading Tumors: Anisotropy and Heterogeneity

Journal:	*Soft Matter*
Manuscript ID	SM-ART-08-2022-001100.R1
Article Type:	Paper
Date Submitted by the Author:	12-Nov-2022
Complete List of Authors:	Naylor, Austin; Oregon State University, Physics Zheng, Yu; Arizona State University Jiao, Yang; Arizona State University, Sun, Bo; Oregon State University, Physics

Soft Matter

ARTICLE TYPE

Cite this: DOI: 00.0000/xxxxxxxxxx

Micromechanical Remodeling of the Extracellular Matrix by Invading Tumors: Anisotropy and Heterogeneity†

Austin Naylor,[a,‡], Yu Zheng,[b,‡] Yang Jiao,[b,c,¶] and Bo Sun[a,¶]

Received Date
Accepted Date

DOI: 00.0000/xxxxxxxxxx

Altered tissue mechanics is an important signature of invasive solid tumors. While the phenomena have been extensively studied by measuring the bulk rheology of the extracellular matrix (ECM) surrounding an tumor, the micromechanical remodeling at the cellular scale remains poorly understood. By combining holographic optical tweezers and confocal microscopy on *in vitro* tumor models, we show that the micromechanics of collagen ECM surrounding an invading tumor demonstrate directional anisotropy, spatial heterogeneity and significant variations in time as tumors invade. To test the cellular mechanisms of ECM micromechanical remodeling, we construct a simple computational model and verify its predictions with experiments. We find that collective force generation of a tumor stiffens the ECM and leads to anisotropic local mechanics such that the extension direction is more rigid than the compression direction. ECM degradation by cell-secreted matrix metalloproteinase softens the ECM, and active traction forces from individual disseminated cells re-stiffen the matrix. Together, these results identify plausible biophysical mechanisms responsible for the remodeled ECM micromechanics surrounding an invading tumor.

Introduction

During the growth and metastasis of solid tumors, reciprocal mechanical interactions between a tumor and its surrounding extracellular matrix (ECM) is of fundamental importance[1]. On one hand, cancer cells apply strong traction forces that cause nonlinear stiffening of ECM[2,3], build up plastic deformations[4–6], to the point of significantly altering the microstructure of the ECM[7,8]. Cancer cells and the cancer associated fibroblasts also secrete matrix metalloproteinase (MMP) that degrades the ECM[9], weakens its structural integrity and even creates hollow tracks along the path of cell migration[10,11]. On the other hand, the remodeled ECM mechanics provides a multitude of physical cues through cell mechanosensing, such that the growth, migration, and malignant transformation are all sensitive to the tumor's mechanical microenvironment[12–17].

Although the mechanics, in particular the bulk rheology of ECM surrounding tumors have been well documented[18–20], and are often studied for their physiological impacts[21], one may recognize the drastic discrepancies in the corresponding scales between rheology and cell-ECM interactions. Bulk rheology characterizes the elastoviscosity of ECM at the millimeter or larger scales, which is appropriate to quantify the overall property of a whole tissue or organism. In contrast, the physical interface between cells and the ECM is no more than a few micrometers in dimension. Therefore a cancer cell will directly modify and respond to the ECM micromechanics at the cellular scale[22–24], and may not have the knowledge of their physical environment at scales hundreds of times larger[25].

The distinct mechanical properties of the ECM at cellular and tissue scales can be traced back to the ECM structure. Collagen ECM, for example, is a disordered assembly of fibrous scaffold with pore sizes ranging from sub-micrometer to a few micrometers[26–28]. These structural features lead to anisotropic and heterogeneous mechanical moduli measured by micrometer-sized probing particles[29–31], or atomic force microscopy[32]. It has been shown that local elasticity can vary by as much as 50% over a distance comparable to a single cell size[29].

Mechanistic understanding of the altered cancer microenvironment requires one to fill the knowledge gap of ECM micromechanics surrounding an invading tumor. To this end, we develop an experimental system that combines confocal imaging, holographic optical tweezers[33,34], and *in vitro* tumor model[35] to quantify the local elastic moduli of ECM outside of disseminating tumor diskoids. We also employ a multiscale computational model[16] that explicitly account for the microscopic structure and physical interactions between cancer cells and 3D ECM. By integrating experiments and the model, we test putative mechanisms that con-

[a] Department of Physics, Oregon State University, Corvallis, OR, USA.
[b] Department of Physics, Arizona State University, Tempe, AZ, USA.
[c] Materials Science and Engineering, Arizona State University, Tempe, AZ, USA.

† Electronic Supplementary Information (ESI) available: [details of any supplementary information available should be included here]. See DOI: 10.1039/cXsm00000x/

‡ These authors contributed equally to this work.

¶ send correspondence to jiao.yang@asu.edu (Y. J.) and sunb@oregonstate.edu (B. S.)

tribute to the anisotropy, heterogeneity, and temporal variations of ECM micromechanics.

Results

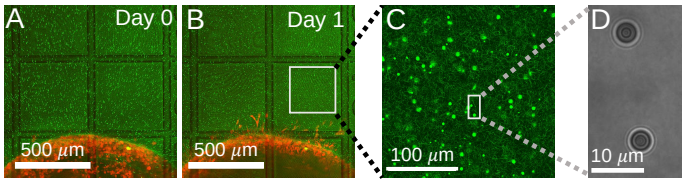

Fig. 1 Microspheres as probing particles are embedded in the extracellular matrix (ECM) surrounding invading tumor diskoids. (A-B) Microscopy images showing MDA-MB-231 cancer cells forming a tumor diskoid (red), with probing particles (green) dispersed in the surrounding ECM, and the sample is mounted on a culture dish with printed grid lines (transmitted light channel). (C) A confocal reflection image showing probing particles (bright spots) inside the collagen matrix (dimmer fibrous structures). (D) A holographic image of probing particles at the optical tweezers setup.

Experimental characterization of ECM micromechanics surrounding an invading tumor.

In order to measure the micromechanics of the extracellular matrix (ECM) surrounding invading solid tumors, we first create tumor diskoids using the DIGME technique we developed previously[35]. This technique precisely control the shape and size of each disk-shaped tumor model, allowing us to combine measurements of multiple tumor samples with fixed geometry. The diskoids consists of MDA-MB-231 cells, a highly invasive line of breast cancer cells that are capable of migrating in 3D ECM. The cells are confined by type-I collagen matrices at a concentration of 2 mg/ml, which contains monodisperse polystyrene microspheres with a diameter of 3 μm as probing particles. Most microspheres are stably embedded in the ECM by attaching to multiple collagen fibers. A small fraction ($\sim$ 10%) of loosely embedded polystyrene particles, likely falling in the space between ECM fibers, are excluded from further measurements. Fig. 1 (A-B) show typical microscopy images of a tumor diskoid over 24 hours of invasion. We culture the diskoid in a gridded culture dish, so that microscopy images at different magnifications or at different days can be correlated. Fig. 1C shows a confocal reflection image of the collagen matrix with the bright spots indicating location of the microspheres. The microsheres uniformly distributes in the ECM. After imaging the diskoid and its ECM on a confocal microscope (Leica SPE), we bring the sample to a home-built holographic optical tweezers (HOT) setup where a high numerical aperture objective lens (100X, NA=1.4) is used to image and optically manipulate the microspheres as probing particles to measure the ECM micromechanics[29].

We choose probing particles at distances less than the radius of the diskoids ($R_s \approx 800$ μm, Fig. 2A), where significant cell-induced ECM deformation is observed. The particles are illuminated by a partial coherent light source, which produces concentric diffraction patterns for high resolution particle tracking[36].

In each measurement, we project optical traps to perturb the probing particle while a nearby unpertubed particle serves as a reference for drift correction (Fig. 2B). Specifically, the probing optical trap is projected at four locations each 1 μm away from the equilibrium position of the particle. The four trap locations are directed radially or tangentially from the diskoid center, which we label as extension (radially outward), compression (radially inward), and shear (tangential) directions. When switching between different microscopes (confocal and HOT), we use the grids printed at the bottom of the culture dish as alignment markers to determine the proper local axis with respect to the tumor diskoid.

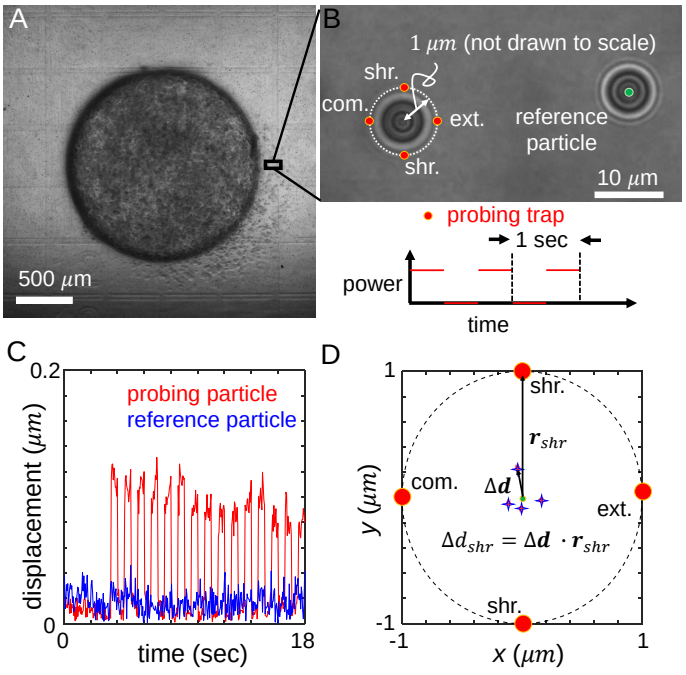

Fig. 2 Measurement of the ECM micromechanics around a invading tumor diskoid via holographic optical tweezers (HOT). (A) A bright field image of a tumor diskoid, where a small section will be investigated on a HOT setup as shown in (B). (B) Semicoherent illumination renders concentric rings around the probing particle and reference particle which facilitate high resolution particle tracking. The optical trap (red dots) are projected in compression (abbreviate com.), extension (abbreviate ext.) and shear (abbreviate shr.) directions 1 μm from the equilibrium position of the probing particle. These directions are defined by the location of the probing particle relative to the center of the tumor diskoid. The power of the optical trap (probing trap) is switches on and off at a frequency of 1 Hz and 50% duty cycle by manipulating the spatial light modulator of the HOT. (C) Representative trajectories of the probing and reference particles showing the displacements from their respective equilibrium positions. (D) Schematics showing the measurement of ECM micromechanics. Red dots: locations of the optical traps in compression, extension and shear directions. Stars: average particle positions in response to optical forces. $\Delta\mathbf{d}$ labels the displacement when the particle is perturbed in the shear direction (with optical trap at $\mathbf{r}_{shr}$).

In order to minimize the measurement error due to mechanical drift and other sources of noise, we cycle the probing trap in the four directions and repeat for 15 times. Along each direction, the power of the optical traps is switched on and off for 0.5 seconds. During the whole process, positions of the reference and probing particles are tracked at a rate of 20 Hz (Fig. 2C), such that the particle displacement in response to optical forces, and the ECM micromechanics derived thereafter, are obtained by

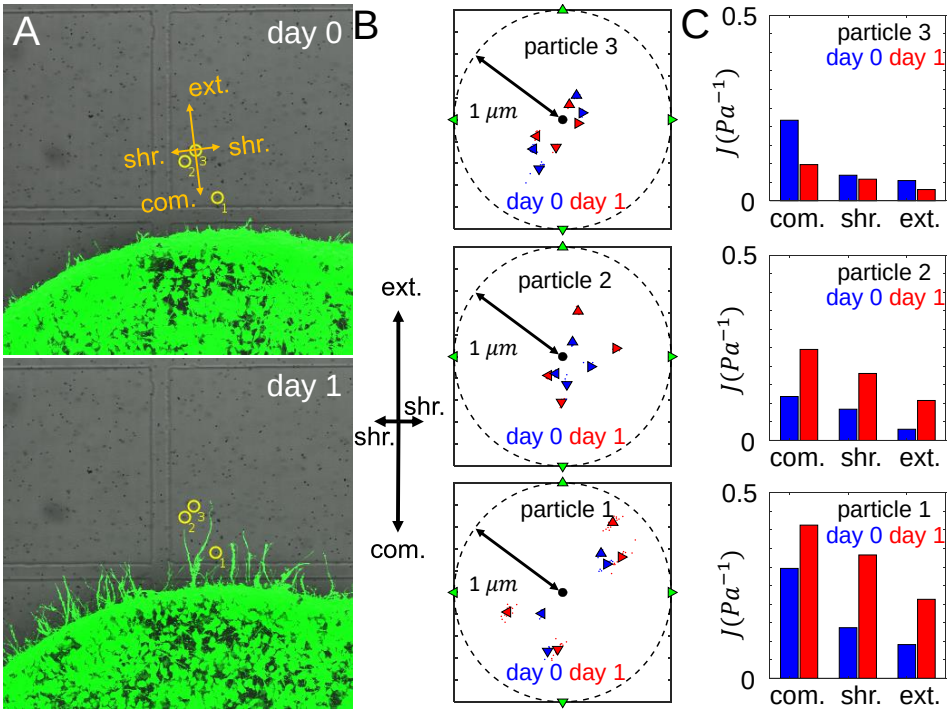

Fig. 3 ECM micromechanics changes over time during tumor invasion. (A) Three probing particles are selected and examined at day 0 and day 1 around the same tumor diskoid. (B) The average displacements of each particle along four probing directions at both day 0 and day 1. (C) The micromechanical compliances measured by each particle at day 0 and day 1.

averaging reference-corrected particle positions for each probing location (Fig. 2D). The particle displacement generally has an off-axis component, and shows strong variations between different probing directions. These phenomena are related with the disordered nature of ECM structure, which are consistent with previous reports of micromechanical measurements in cell-free matrices[29]. The on-axis displacements, such as Δd_{shr} as shown in Fig. 2D, will allow us to compute the local mechanical modulus. Note that to account for the finite particle response time to optical forces, we exclude particle trajectories at the boundaries of each power cycle (4-6 frames) when computing the average particle displacements.

ECM Micromechanics is Remodeled by Invading Tumors.

To quantify the ECM micromechanical remodeling by an invading tumor, we first focus on micromechanics measured by the same set of particles over 24 hours of invasion. Fig. 3A shows three probing particles with distances ranging between 80 μm and 180 μm to the boundary of a diskoid. For each particle, we project optical traps in the extension, compression and shear directions with respect to the diskoid, and obtain the reference-corrected displacements. Note that the off-axis displacements and anisotropy are evident for all three particles.

Along each probing direction, we calculate the directional compliance :

$$J_{dir} = 6\pi a \frac{\Delta d_{dir}}{F_{dir}} \quad (1)$$

where dir refers to one of the four probing directions (extension, compression and shear), $a = 1.5\mu$m is the particle radius, Δd_{dir} is the component of the particle displacement along the probing direction, F_{dir} is the component of the optical force along the probing direction. The optical force is calculated by approximating the optical trap as a harmonic spring, whose stiffness is calibrated to be 50 pN/μm. For the shear compliance, we further take the average of the two symmetric shear directions.

The directional compliance reported by the three particles are significantly different from each other. For instance particle 1 measures a local compression compliance of 0.3 Pa^{-1} at day 0, corresponding to local stiffness of 3.3 Pa. This is almost three times softer than the compression modulus reported by particle 2. On the other hand, the micromechanics measured by particle 3 is stiffest in the shear direction, while particle 1 and 2 show the micromechanics are most stiff in the extension direction. The temporal evolution also differs for the three particle locations: while particle 1 and 2 show ECM softens in all directions from day 0 to day 1, particle 3 exhibit the opposite trend. In fact, ECM at particle 2 is softened by more than doubling the compliance, while its nearby particle 3 shows modest stiffening after 24 hours of diskoid invasion. These results highlight the heterogeneity of ECM micromechanics, which would be elusive if we only had the information of bulk rheology.

Computational modeling of ECM micromechanics surrounding an invading tumor.

In order to test putative physical mechanisms contributing to the ECM micromechanical remodeling, We employ a nonlinear model of the ECM network[37], in which the structure of the network is represented as a disordered 3D graph. The bonds represent fiber segments and the nodes in the graph represent cross-

links. The graph was reconstructed from confocal images of 2 mg/ml collagen[37,38], corresponding to an average bond length of $\sim 1.8\ \mu m$. Upon stretching, a fiber segment (bond) first elongates elastically, which is followed by strong strain-hardening once the elongation is larger than a prescribed threshold. Upon compression, the fiber buckles and possesses a much smaller compression modulus. The elongation stiffness k of the fiber is accordingly given by

$$k = \begin{cases} \rho EA, & \lambda < 0 \\ EA, & 0 < \lambda < \lambda_s \\ EA\exp[(\lambda - \lambda_s)/\lambda_0], & \lambda > \lambda_s. \end{cases} \quad (2)$$

where E and A are respectively the Young's modulus and cross-sectional area of the fiber bundle, and we use $EA = 8 \times 10^{-7} N$[26]; $\lambda = \delta\ell/\ell$ is elongation strain, and $\lambda_s = 0.02$ and $\lambda_0 = 0.05$ are parameters for the strain-hardening model[39]; $\rho = 0.06$ describes the effects of buckling[40]. This model has been validated to realistically capture the mechanical behaviors of collagen networks in responses to cellular forces[16,22,37]. In its current form, we do not explicitly consider the time-dependent behaviors of the fibers, such as creep and plasticity.

We model a diskoid embedded in the ECM as a short cylinder with radius $R_s = 250\ \mu m$ and height $h = 80\ \mu m$ and with the height along the z axis. The cylinder is placed at the center of a representative volume element (RVE) with dimensions $1500\ \mu m \times 1500\ \mu m \times 400\ \mu m$ along x, y, and z direction respectively (see Fig. 4A). Although the simulation system is smaller compared to the experimental system due to computational cost, we expect the system size is sufficiently large to obtain at least qualitative insights of the physics behind the experimental observations. The contraction of the diskoid pulls the nodes residing within the diskoid region (i.e., the cylinder) towards the center along the radial direction, which is modeled by an affine transformation with a contraction ratio γ. In the subsequent simulations, we use $\gamma = 0.93$, as calibrated from experimental imaging data. After diskoid contraction, a force-based relaxation method is employed to obtain the force-equilibrium network configuration and resolve the forces on each fiber[37].

The micromechanical compliance is measured following a similar but slightly different procedure used in the experiment. Specifically, spherical beads of radius $a = 1.5\ \mu m$ are randomly introduced in the ECM, one at a time. A bead is subsequently displaced along the extension, compression and shear directions by $\Delta d_{dir} = 1\ \mu m$. We also investigate $\Delta d_{dir} = 0.1\ \mu m$ and $0.01\ \mu m$ and verify the obtained directional compliance values are not sensitive to d_{dir} (see Supplementary Information). Under this fixed displacement condition, the total response force F_{dir} on the bead along the corresponding direction is obtained from the force-equilibrium network configuration. The corresponding compliance J_{dir} is then computed following Eq. (1), see Fig. 4B).

ECM micromechanical anisotropy resulted from the collective traction force of a tumor.

We first use the simulation to investigate the interplay of ECM nonlinear mechanics and the collective contractile force generated by a tumor. Figure 5A shows the average elongation strain $\bar{\lambda}$ of tensile fibers in the ECM as a function of D/R_s, where D is the distance to the tumor boundary, and R_s is the radius of the tumor. In the nonlinear fiber model, we consider fibers enter the strain-hardening regime once $\lambda > \lambda_s = 0.02$. It can be seen that in the vicinity of tumor surface (e.g., $D \leq 0.2R_s$), $\bar{\lambda} > \lambda_s$, indicating that the majority of tensile fibers in this region are in the strain-hardening regime. As D increases beyond this region, $\bar{\lambda}$ decreases quickly. However, as shown in Fig. 5B, there are still significant fractions of tensile fibers that are in the strain-hardening regime in the region with $D < R_s/2$.

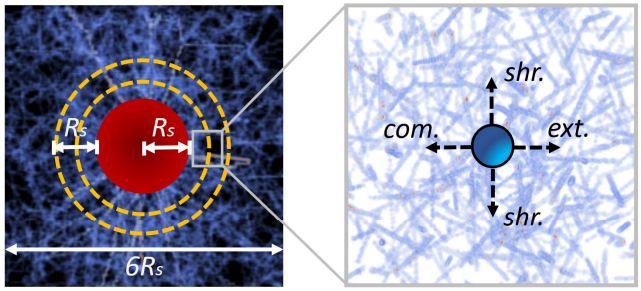

Fig. 4 Illustration of the simulation model to investigate the ECM micromechanical remodeling by an invading tumor. (A) A schematic showing the simulation representative volume element (RVE). (B) Micromechanics is quantified by measuring the directional compliance as in the experiments.

The average directional compliance obtained from simulations are shown in Fig. 5 (C-D). It can be seen that in the near-tumor region ($D < R_s/2$), the directional compliance exhibits strong anistropy. Specifically, the extension compliance is smaller than the shear compliance, and significantly smaller than the compression compliance. This equivalently indicates that the extension stiffness is larger than the shear stiffness, and much higher than the compression stiffness. This trend is resulted from the strong strain hardening of tensile fibers in the region, which dominates the micromechanics. Specifically, when the probing bead is displaced in the tension direction, the tensile fibers already in the strain hardening regime are further pulled longer, leading to a strong and fast increasing response force, and thus, a high stiffness or low compliance. On the other hand, displacing the bead in the compression direction releases the tensile strain in the fibers, resulting in a much lower stiffness or higher compliance. Measuring the shear compliance amounts to pulling the tensile fibers sideways, with only a small component along the tensile direction, thus leading to a stiffness lower than the tension case, but higher than the compression case. Similar trend is observed in the far region ($D > R_s/2$), albeit the distinctions between the compliance (stiffness) are less apparent as those in the near-tumor region. This is because the strain hardening effects in the far region are significantly weaker (see Fig. 5B).

ECM degradation by cancer cells softens the ECM.

Once the tumor invasion starts, cancer cells such as MDA-MB-231 cells secrete matrix metalloproteinase (MMPs) to degrade the

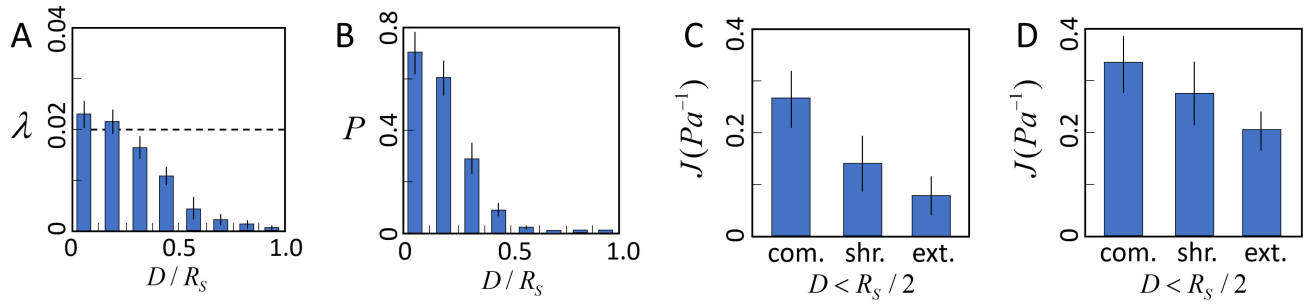

Fig. 5 The tensile stress generated by the tumor coupled with the nonlinear elasticity of the ECM leads to anisotropic micromechanical properties in the ECM. (A) Average elongation strain $\lambda = \delta\ell/\ell$ of tensile fibers in the ECM as a function of distance D/R_s from tumor surface (dashed line indicates the critical elongation strain $\lambda_s = 0.02$ for strain hardening). Here D is the distance to the tumor boundary, and R_s is the radius of the tumor. (B) Fraction P of tensile fibers that are in the hardening regime as a function of distance D/R_s from tumor surface. (C) Average compliance J_{dir} along different directions in the region with $D < R_s/2$. (D) Average compliance J_{dir} along different directions in the region with $D > R_s/2$. In (A-D) errorbars show standard deviation of simulation results.

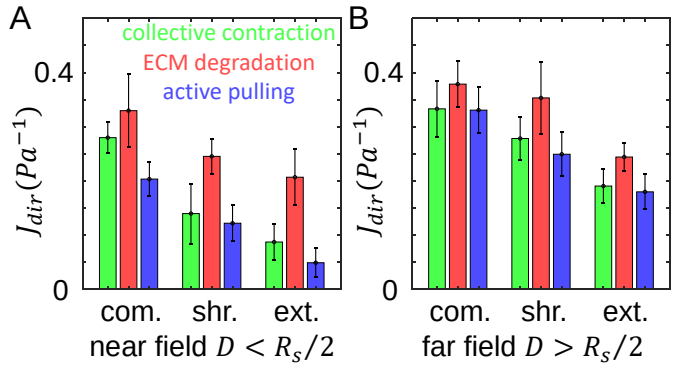

Fig. 6 The directional compliance of the ECM from simulations. (A) Directional compliance J_{dir} along different directions in the near field with $D < R_s/2$, where D is the distance to the tumor boundary, and R_s is the radius of the tumor. (B) Directional compliance J_{dir} in the far field with $D > R_s/2$. Green: results by taking into account of the collective contraction of the tumor (same as Fig. 5). Red: results when the tumor's collective contraction and ECM degradation are both considered. Blue: results when tumor's collective contraction, ECM degradation and a nearby cell's active pulling are all considered.

ECM fibers and damage the structural integrity of network. This effect is likely reflected by the measured compliance for particles 1 and 2, for which the day 1 values of directional compliance J_{dir} are higher than the corresponding day 0 values (Fig. 3C). Here we use simulations to further verify this effect. In particular, for a given bead we first obtain J_{dir} as in the previous section. Subsequently, we set the fiber segments within $\delta = 2$ μm along the line that connects the tumor center and the bead to have a much lower elongation stiffness than the original value, i.e., $k = 0.01 \cdot EA$, which also does not possess strain hardening effect. This is to mimic the effects of ECM degradation by invasive cells that produce weak micro-channels in the ECM network. The values of J_{dir} are then computed again. We repeat the procedure for different beads in both near and far regions.

Figure 6 shows computed average J_{dir} along different directions in both near and far regions before (green bars) and after ECM degradation (red bars). It can be clearly seen that all J_{dir} increase after degradation, while the trend $J_{ext} < J_{shr} < J_{com}$ is preserved. This is consistent with the experimental observations for particles 1 and 2 (see Fig. 3C).

Active pulling by disseminated cancer cells stiffens the ECM.

The directional compliance J_{dir} at particle 3 (Fig. 3C) exhibit very interesting behavior. Specifically, the values of J_{dir} on day 1 decrease compared to the corresponding values on day 0, indicating the ECM is locally stiffened. A closer examination of Fig. 3A reveals that on day 1, an branch of invading cell extends to the region near particle 3 (but not directly in front of the particle, as in the case of particle 2). As the cells at the invasion front lead the migration, they can generate contractile forces that reinforce the collective contraction of the tumor. Again we use simulations to verify this effect. For a given bead, we first obtain J_{dir} as in the previous section. Next, we embed a spherical cell of diameter 15 μm in a random location that is 10 μm away from the bead (as estimated from the imaging data). The cell is contracted by 15%, which pull the near-by fibers. The resulting J_{dir} are then computed and this procedure is repeated for all beads.

Figure 6 shows computed mean J_{dir} along different directions in both near and far regions after additionally taking into account of active pulling forces by nearby disseminated cancer cells (blue bars). It can be clearly seen that all J_{dir} decrease due to cell contraction, while the trend $J_{ext} < J_{shr} < J_{com}$ is still preserved. This is consistent with the experimental observations for particles 3 (see Fig. 3C). Together, these simulation results demonstrate effects of various mechanisms where the ECM micromechanics can be remodeled by both the whole tumor and individual disseminated cancer cells.

Further experimental verification of model predictions.

Our computational model predicts several features in addition to the heterogeneity of the ECM micromechanics. To test these predictions experimentally, we leverage the precision shape control of DIGME technique and accumulate data from multiple diskoids with the same radius. In particular, we perform micromechanical measurements on 10 diskoids at day 0 and another 10 at day 1. For each sample, we select approximately 10 probing parti-

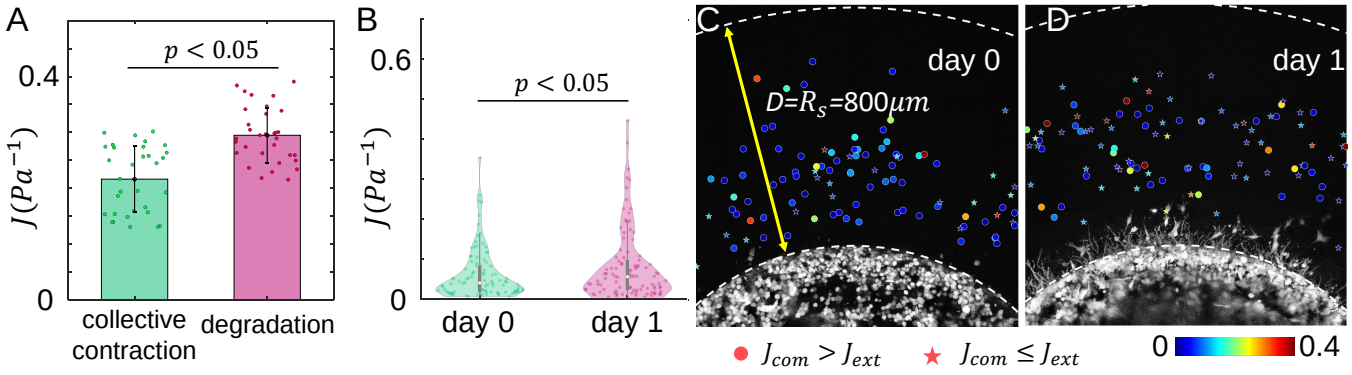

Fig. 7 The temporal evolution of ECM micromechanics. (A) Our computational model predicts the ECM compliance J increases as ECM degradation by invading cancer cells takes place. Errorbars: standard deviations. (B) Experimentally measured ECM compliance at day 0 and day 1. The violin plots show the distribution functions. Statistical comparison in A and B are done with one way ANOVA. (C-D) ECM micromechanical measurements surrounding tumor diskoids are combined from multiple samples at day 0 (C) and day 1 (D). Here scattered dots are color coded by the micromechanical compliance J. circular symbols show measurements where $J_{com} > J_{ext}$, star symbols show measurements where $J_{com} \leq J_{ext}$ Taking advantage of the circular symmetry, the radial positions of the particles are actual measured distances from diskoid centers, while the angular positions of the particles are artificially randomized.

cles with distances from the diskoid ranging from 100 to 700 μm, and close to the same focal plane as the diskoid center. We measure the local mechanics in the extension, compression and shear directions, and define the (mean) micromechanical compliance J as the average of J_{dir} in all four directions:

$$J = \frac{1}{4}(J_{com} + J_{ext} + 2J_{shr}) \quad (3)$$

Our model predicts that ECM degradation by an invading tumor softens the surrounding ECM. This is case for both directional compliance J_{dir} (Fig. 6) as well as the mean compliance J (Fig. 7A). Experimentally, we expect effects of ECM degradation emerge after 24 hours of invasion. Consistent with the model prediction, the micromechanical compliance J measured at at day 1 is generally softer than at day 0 (Fig. 7B). Interestingly, the measured J follow distributions exhibiting long tails, which appear to be distinct from the model calculation.

Our model also predicts that the ECM is stiffer in the extension direction than in the compression direction due to the collective contraction of the tumor, and the difference is less pronounced when ECM degradation takes place (Fig. 6). Experimentally, at day 0 we find $J_{com} > J_{ext}$ in 75% of the instances. In contrast, only 45% measurements at day 1 show $J_{com} > J_{ext}$. These results again qualitatively agree with the model predictions.

Conclusion and Discussions

The growth and metastasis of solid tumors involve significant mechanical remodeling of the surrounding tissue[41]. Reciprocally, the altered tissue provide physical cues to the cancer cells through their mechanosensing pathways to modulate the cancer cell biology[42]. Here we combine experiments and computational modeling to investigate mechanisms with which an invading tumor remodels the elastic properties of the extracellular matrix.

In order to provide insights to physiologically relevant tissue mechanics at the cellular scale, we focus on the micromechanics, rather than the extensively studied bulk rheology of the ECM. To measure the ECM micromechanics, We employ holographic optical tweezers coupled with confocal microscopy (Fig. 1 - Fig. 2). We create *in vitro* models of solid tumors by forming breast cancer diskoids in 3D collagen ECM. The circular symmetry differentiates the tissue space outside of the tumor into compression, shear, and extension directions, along which we probe the ECM local elasticity respectively. We find that the micromechanics of ECM surrounding an invading tumor demonstrate anisotropy in the directions probed, strong heterogeneity in space and also variations in time (Fig. 3). These results are difficult, if not impossible, to derive from bulk rheology alone. To our knowledge, detailed ECM micromechanics in proximity to a disseminating tumor has been a challenge to measure directly. We notice that the ECM micromechanical properties we have measured indicated a softer ECM compared to that suggested by a recent report of active microrheology results[43]. We suspect differences in the probing frequency, and spatial statistics may contribute to the difference in the moduli measured via these two distinct techniques. This also indicates the important nonlinear dynamic-dependent micromechanics of ECM, which should be taken into account for understanding its mechanical interaction with active cells. For future research it will be interesting to combine multiple micromechanical characterizations to better understand the physical properties of tumor associated ECM.

With a simple numerical model, we propose three independent and additive cellular mechanisms to account for the strong micromechanical heterogeneity observed in experiments. As we and other groups have reported previously, collective traction forces of the cells lead to global contraction of the ECM toward the tumor center[44]. Models based on bulk rheology suggest that in regions close to the tumor ECM elastic moduli will increase due to the strain-stiffening effect[3]. Our micromechanical model, on the other hand, predicts that ECM is stiffened more in the extension direction compared to the compression direction (Fig. 5 - Fig. 6). This prediction is well supported by the experiments (Fig. 7).

Mesenchymal cancer cells, such as MDA-MB-231 cells generally

execute MMP-dependent programs of 3D migration[45,46]. During mesenchymal migration, cells secrete MMPs that degrade the ECM. Our model predicts and experiments confirm that ECM degradation softens the ECM micromechanics (Fig. 6 - Fig. 7). As individual cells further disseminate into the ECM, their traction force will actively pull on the nearby matrix, resulting in local stiffening. However, this latter effect depends on the location and orientation of the force-generating cell, therefore may further contribute to the level of heterogeneity and temporal variations in the ECM micromechanics.

While the predictions from our simplified model qualitatively agree with experiments, admittedly there are several notable discrepancies. For instance, the experimentally measured distribution of mean compliance J is approximately log-normal, which is broader compared with the distribution calculated from the model. Additionally, at day 1 of invasion only 45% of measured instances show $J_{com} > J_{ext}$, while the model predicts the compression compliance to be greater than extension compliance. The discrepancies could be attributed to a number of overlooked factors, such as the plasticity of the ECM at high strains[6], as well as the dynamic phases of cell migration and force generation[47]. Recently, it is shown that MDA-MB-231 cells exhibit transitions between multiple migrational phenotypes[48,49]. We expect the phenotypical plasticity further contribute to variations of cellular force generated and the stress state of the ECM. It is interesting for future research to include more detailed cellular dynamics and mechanosensivity in order to better model the physical interactions of invading tumors and their host tissue[50].

Author Contributions

Y. J. and B. S. initiated the research. A.N. conducted the experiments. Y. Z. and Y. J. constructed the computational model. All authors analyzed data and wrote the manuscript.

Conflicts of interest

There are no conflicts to declare.

Acknowledgements

The work is supported by Department of Defense award W81XWH-20-1-0444 (BC190068) to A. N., the National Institute of General Medical Sciences award 1R35GM138179 to B. S.. Y. Z. and Y. J. are supported by National Science Foundation under grant No. 1916878.

Notes and references

1 P. Friedl and S. Alexander, *Cell*, 2011, **147**, 992–1009.

2 H. Wang, A. S. Abhilash, C. S. Chen, R. G. Wells and V. B. Shenoy, *Biophys. J.*, 2014, **107**, 2592.

3 M. S. Hall, F. Alisafaei, E. Ban, X. Feng, C.-Y. Hui, V. B. Shenoy and M. Wu, *Proceedings of the National Academy of Sciences*, 2016, **113**, 14043–14048.

4 S. Nam, K. H. Hu, M. J. Butte and O. Chaudhuri, *Proc. Natl. Acad. Sci.*, 2016, **113**, 5492.

5 S. Nam, J. Lee, D. G. Brownfield and O. Chaudhuri, *Biophys. J.*, 2016, **111**, 2296.

6 J. Kim, J. Feng, C. A. R. Jones, X. Mao, L. M. Sander, H. Levine and B. Sun, *Nature Communications*, 2017, **8**, 842.

7 Q. Shi, R. P. Ghosh, H. Engelke, C. H. Rycroft, L. Cassereau, J. A. Sethian, V. M. Weaver and J. T. Liphardt, *Proc. Natl. Acad. Sci*, 2014, **111**, 658–663.

8 J. WH, Y. N, C. CC, E. K, H. B and C. Y., *Biomaterials*, 2020, **234**, 119756.

9 K. Wolf, Y. I. Wu, Y. Liu, J. Geiger, E. Tam, C. Overall, M. S. Stack and P. Friedl, *Nat. Cell Biol.*, 2007, **9**, 893.

10 C. Gaggioli, S. Hooper, C. Hidalgo-Carcedo, R. Grosse, J. F. Marshall, K. Harrington and E. Sahai, *Nat. Cell Biol.*, 2007, **9**, 1392–1400.

11 A. Glentis, P. Oertle, P. Mariani, A. Chikina, F. El Marjou, Y. Attieh, F. Zaccarini, M. Lae, D. Loew, F. Dingli, P. Sirven, M. Schoumacher, B. G. Gurchenkov, M. Plodinec and D. M. Vignjevic, *Nat. Comm.*, 2017, **8**,.

12 D. Kim, P. P. Provenzano, C. L. Smith and A. Levchenko, *J. Cell Biol.*, 2012, **197**, 351.

13 R. Fernandez-Gonzalez, M. S. Simoes, J. C. Röper, S. Eaton and J. A. Zallen, *Dev. Cell*, 2009, **17**, 736–743.

14 T. Lecuit, P. Lenne and E. Munro, *Annu. Rev. Cell Dev. Biol.*, 2011, **27**, 157–184.

15 H. Ahmadzadeh, M. R. Webster, R. Behera, A. M. J. Valencia, D. Wirtz, A. T. Weeraratna and V. B. Shenoy, *Proceedings of the National Academy of Sciences*, 2017, **114**, E1617–E1626.

16 J. Kim, Y. Zheng, A. A. Alobaidi, H. Nan, J. Tian, Y. Jiao and B. Sun, *Biophysical J.*, 2020, **18**, 1177.

17 K. W, F. J, S. CP, H. YL, S. Y, K. SA, M. JA, K. A, B. JP, R. D, Z. MH, P. JA, G. M, C. Z, P. AF and F. JJ., *iScience*, 2021, **24**, 103252.

18 Y. Yang, L. M. Leone and L. J. Kaufman, *Biophys. J.*, 2009, **97**, 2051–60.

19 C. P. Broedersz and F. C. MacKintosh, *Rev. Mod. Phys.*, 2014, **86**, 995.

20 J. Feng, H. Levine, X. Mao and L. M. Sander, *Soft Matter*, 2016, **12**, 1419–1424.

21 A. I, C. L, D. I, S. Q, A. A, P. C, C. YY, L. J, H. ES and W. VM., *Integr Biol*, 2015, **7**, 1120.

22 Y. Zheng, H. Nan, Q. Fan, X. Wang, L. Liu, R. Liu, F. Ye, B. Sun and Y. Jiao, *Phys. Rev. E*, 2019, **100**, 043303.

23 F. J. O'Brien, B. A. Harley, I. V. Yannas and L. J. Gibson, *Biomaterials*, 2005, **26**, 433–441.

24 B. M. Baker and C. S. Chen, *J. Cell Sci.*, 2012, **125**, 3015–3024.

25 M. Proestaki, B. M. Burkel, E. E. Galles, S. P. Ponik, and J. Notbohm, *Soft Matter*, 2021, **17**, 10263.

26 S. B. Lindström, D. A. Vader, A. Kulachenko and D. A. Weitz, *Phys. Rev. E*, 2010, **82**, 051905.

27 C. A. Jones, L. Liang, D. Lin, Y. Jiao and B. Sun, *Soft Matter*, 2014, **10**, 8855–8863.

28 B. Sun, *Cell Reports Physical Science*, 2021, **2**, 100515.

29 C. A. R. Jones, M. Cibula, J. Feng, E. A. Krnacik, D. H. McIntyre, H. Levine and B. Sun, *Proc. Natl. Acad. Sci.*, 2015, **112**, E5117.

30 S. JR, V. W, F. KL, L. R, D. A and T. K., *Cell Mol Bioeng.*, 2016, **9**, 398.

31 Y. L. Han, P. Ronceray, G. Xu, A. Malandrino, R. D. Kamm, M. Lenz, C. P. Broedersz and M. Guo, *Proceedings of the National Academy of Sciences*, 2018, **115**, 4075–4080.

32 A. D. Doyle, N. Carvajal, A. Jin, K. Matsumoto and K. M. Yamada, *Nat. Comm.*, 2015, **6**, 8720.

33 D. G. Grier, *Nature*, 2003, **424**, 810–816.

34 D. G. Grier and Y. Roichman, *Applied Optics*, 2006, **45**, 880–887.

35 A. A. Alobaidi and B. Sun, *Cancer Convergence*, 2017, **1**, 1.

36 R. Parthasarathy, *Nat. Methods*, 2012, **9**, 724–726.

37 L. Liang, C. A. Jones, S. Chen, B. Sun and Y. Jiao, *Physical Biology*, 2016, **13**, 066001.

38 H. Nan, L. Liang, G. Chen, L. Liu, R. Liu and Y. Jiao, *Physical Review E*, 2018, **97**, 033311.

39 J. Steinwachs, C. Metzner, K. Skodzek, N. Lang, I. Thievessen, C. Mark, S. Münster, K. E. Aifantis and B. Fabry, *Nature methods*, 2016, **13**, 171–176.

40 J. Notbohm, A. Lesman, P. Rosakis, D. A. Tirrell and G. Ravichandran, *Journal of The Royal Society Interface*, 2015, **12**, 20150320.

41 M. Egeblad, M. G. Rasch and V. M. Weaver, *Curr. Opin. Cell Biol.*, 2010, **22**, 697.

42 A. M, S. L and W. H., *Cancers (Basel)*, 2021, **13**, 4754.

43 A. Jagiełło, M. Lim and E. Botvinick, *APL Bioengineering*, 2020, **4**, 046105.

44 A. A. Alobaidi, Y. Xu, S. Chen, Y. Jiao and B. Sun, *Physical Biology*, 2017, **14**, 045005.

45 K. E. Fisher, A. Sacharidou, A. N. Stratman, A. M. Mayo, S. B. Mayo, S. B. Fisher, R. D. Mahan, M. J. Davis and G. E. Davis, *J. Cell Sci.*, 2009, **122**, 4558–4569.

46 R. J. Petrie and K. M. Yamada, *J. Cell Science*, 2012, **125**, 5917–5926.

47 K. Vaidžiulytė, A.-S. Macé, A. Battistella, W. Beng, K. Schauer and M. Coppey, *eLife*, 2022, **11**, e69229.

48 C. z Eddy, H. Raposo, A. Manchanda, R. Wong, F. Li and B. Sun, *Scientific Reports*, 2021, **11**, 20434.

49 J. Kim, Y. Cao, C. z Eddy, Y. Deng, H. Levine, W.-J. Rappel and B. Sun, *Proceedings of the National Academy of Science*, 2021, **118**, e2024780118.

50 X. Chen, D. Chen, E. Ban, K. C. Toussaint, P. A. Janmey, R. G. Wells and V. B. Shenoy, *Proceedings of the National Academy of Sciences*, 2022, **119**, e2116718119.